

Chapter 2

Stellar Activity as a Source of Radial-Velocity Variability

The key to breaking the activity barrier in exoplanet detections lies in our understanding of the physical origin and temporal structure of stellar RV variability. This chapter provides a review of the manifestations of magnetic activity, their impact on photometric and spectroscopic observations, and the analysis techniques that have been developed in recent years to account for activity-induced RV signals. I also present the target selection criteria I proposed to pick “magnetically manageable” stars for HARPS-N RV follow-up.

The signatures of magnetic activity span a wide range of spatial and temporal scales. We tend to naturally think of things in terms of their physical sizes. But when it comes to looking at stars, we see them as minuscule point-like objects in the night sky, and it is impossible to observe their surfaces with high resolution (except for the Sun). We can thus only gather limited information about spatial structures on the stellar surfaces.

The time-dependent nature of observations allows us to watch the surfaces of stars change and evolve over time and thus form a detailed picture of the various time scales at play. The temporal structure of the signals we observe can tell us a lot about the stars they originate from. In the first part of this chapter, I will present each stellar activity timescale, starting from acoustic oscillations that evolve within minutes, up to magnetic cycles that last decades.

2.1 Magnetic Activity and Its Manifestations

Before we look at the temporal and spatial diversity of magnetic activity signatures, however, let us catch a glimpse at how magnetic fields are produced within stars. It has long been found that a dynamo process operates within the stellar interior (Babcock 1961; Parker 1963, see Tobias 2002 and references therein). Over recent years, helioseismic studies and sophisticated numerical models have taught us much

about the Sun's internal dynamics, although much debate remains (see review by Charbonneau 2010). Current theories of solar dynamo processes are detailed in Choudhuri (2007).

The Sun, like all stars, generates energy in its core through the process of nuclear fusion. This energy is carried outwards in the form of radiation through the radiative zone, where photons undergo a random walk which takes about 10 million years (Lockwood 2005). The radiative zone constitutes the majority of the Sun's interior. Above it lies a convective zone which takes up around 30 % of the interior (in radius). In less massive stars, the radiative layer is thinner or may not be present at all—for stars with masses less than $0.35 M_{\odot}$ (corresponding to early M spectral type), convection is the dominant mechanism for energy transport throughout the star (Hansen and Kawaler 1994; Chabrier and Baraffe 1997). Hot fluid cells are driven upwards due to buoyancy forces. The cells cool when they reach the stellar surface and eventually sink back, and so on.

In Sun-like stars, the radiative and convective layers are separated from each other by a thin layer called the tachocline (Spiegel and Zahn 1992; Miesch 2005). In this region, strong radial shearing forces arise due to the transition between the uniformly rotating radiative zone and the differentially rotating convection zone. It is now generally accepted that this shear is the source of the stellar magnetic dynamo, which is responsible for stellar activity (Tobias 2002). Fully convective stars, in which there is no tachocline, have a different type of dynamo which can result in both basic magnetic field topologies (Morin et al. 2008) or very complex ones (Chabrier and Küker 2006). Fully radiative stars have very weak and unordered fields, if any, and it is unclear how they are created (see Walder et al. 2012 and references therein). A small subset, however, such as the chemically peculiar A stars, have very strong magnetic fields, but these appear to be fossil fields rather than dynamo-generated. Their configurations do not change with time (see Aurière et al. 2014 and references therein).

Light escapes from stars in the bottom layer of the stellar atmosphere: the photosphere. Above the photosphere lies the chromosphere, which is surrounded by the corona, which extends out into space through the solar wind. The photosphere is commonly regarded as the stellar surface and is peppered with granulation, spots and faculae: these are some of the signatures of stellar magnetic activity.

Useful textbooks and reviews on the topics covered in this chapter include Rutten and Schrijver (1994)—proceedings of *Solar Surface Magnetism*,¹ Schrijver and Zwaan (2000)—a book on solar and stellar magnetic activity, Hall (2008)—a review on chromospheric activity, and Reiners (2012)—a review on observations of magnetic fields in Sun-like stars. A great place to find general reviews and articles on solar and stellar activity is the *Living Reviews in Solar Physics*.² For more general information on stellar interiors and atmospheres, two classic textbooks are Novotny

¹NATO Advanced Research Workshop, held in the Netherlands in 1993.

²Published by the Max-Planck-Institut für Sonnensystemforschung, Germany. Available online at: <http://solarphysics.livingreviews.org/>.

(1971) and Gray (1992). I also provide more specific references throughout this chapter.

2.1.1 Minutes: Oscillations

Stars breathe. Their internal pressure constantly fluctuates by tiny amounts; this creates acoustic waves going through the star's interior, which result in the formation of ripples on the stellar surface. These waves were first observed on the Sun by Leighton et al. (1962); later on, Bedding et al. (2001) reported on the first clear detection of similar oscillations in a star other than the Sun, α Cen A. These oscillations, commonly known as p-modes, repeat on timescales of about 5–15 min and produce RV oscillations with an amplitude of a few $\text{m} \cdot \text{s}^{-1}$.

To illustrate this, I retrieved RV observations of the bright Sun-like star μ Arae, taken at a 2-min cadence over an 8-night run for an asteroseismic study (Bouchy et al. 2005). The RV variations recorded on one of the nights are plotted in Fig. 2.1. The p-mode oscillations are clearly visible, particularly in panel (c), which shows a close-up on an oscillation with a period of about 8 min. We can confirm the presence of this signal by looking at the Lomb–Scargle periodogram (Lomb 1976; Scargle 1982; Zechmeister and Kürster 2009; see Sect. 2.3.2.1) of the dataset, displayed in Fig. 2.2. We also see other peaks at 5 and 11 min, which arise from p-mode oscillations that have a slightly different frequency.

We can average out the RV effects of these short frequency oscillations simply by making sure our observations are at least 10 min long (Dumusque et al. 2010). It is common practice with HARPS and HARPS-N to make 15-min observations in order to cancel their effect.

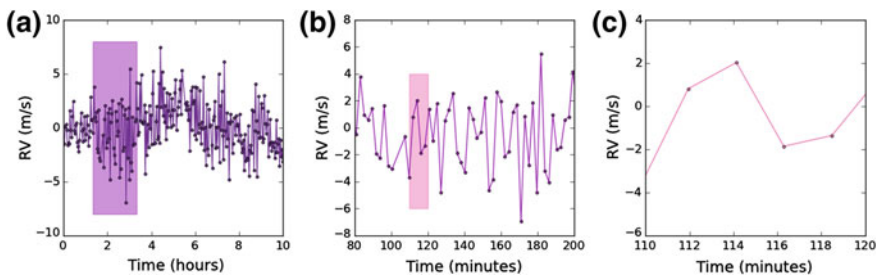


Fig. 2.1 RV observations of the bright star μ Arae (also known as HD 160691, $V = 5.1$ mag), monitored at high-cadence (100-s exposures with 31-s of dead time in between) as part of an 8-night HARPS run in June 2004 (ESO program 073.D-0578, Bouchy et al. 2005). Panel **a** shows observations made over one night. Panel **b** is a zoom-in over a 2 h period, and panel **c** is a zoom-in over 10 min. Panel **a** clearly shows the 2-h granulation signal, while panels **b** and **c** highlight the p-modes

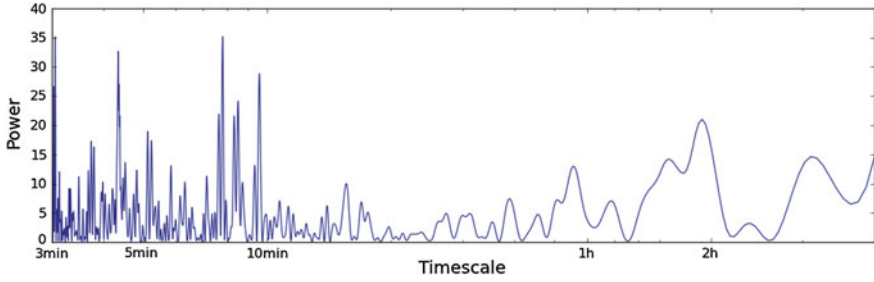


Fig. 2.2 Lomb–Scargle periodogram of the RVs of μ Arae plotted in Fig. 2.1. The strong peaks close to 4 and 8 min are caused by the p-modes, while the peak at about 2 h is due to granulation motions

2.1.2 Minutes: Flares and Coronal Mass Ejections

The magnetic energy stored in active regions and their surroundings can lead to sudden releases in the form of large eruptions known as flares or coronal mass ejections (see Hathaway 2010 and references therein). These events lead to sudden and sharp increases of brightness, and have been observed on other Sun-like stars in *Kepler* lightcurves (see Walkowicz et al. 2011 and others).

These dramatic events are rare in the sort of low-activity stars suitable for planetary RV searches, and easily identified in RV observations as they will generate spikes of several tens of $\text{m} \cdot \text{s}^{-1}$ in the mean RV variations of a star, and show strong signatures in the $\text{H}\alpha$ emission profile (Reiners 2009).

2.1.3 Minutes to Hours: Granulation

A small patch of the Sun’s surface is pictured in Fig. 2.3, revealing the bright and dark granulation structures in impressive detail. This pattern originates from the convective motions taking place below the surface: hot fluid cells rise up to the surface, forming large and bright patches, which sink once they have cooled and become dense enough for gravity to pull them back down.

Granules have a diameter of a few hundred kilometres, and a lifetime of the order of about 8 min (Bahng and Schwarzschild 1961; Hall 2008). There also exist larger structures called mesogranules; these have lifetimes of 30–40 min (Roudier et al. 1998). The largest convective cells, known as supergranules, have sizes of order 40–50 Mm and remain on the stellar surface for about a day (Del Moro et al. 2004).

This short frequency bustling leads to variations in brightness, which we can now easily probe on Sun-like stars thanks to high precision, short cadence *Kepler* photometry (Gilliland et al. 2011).

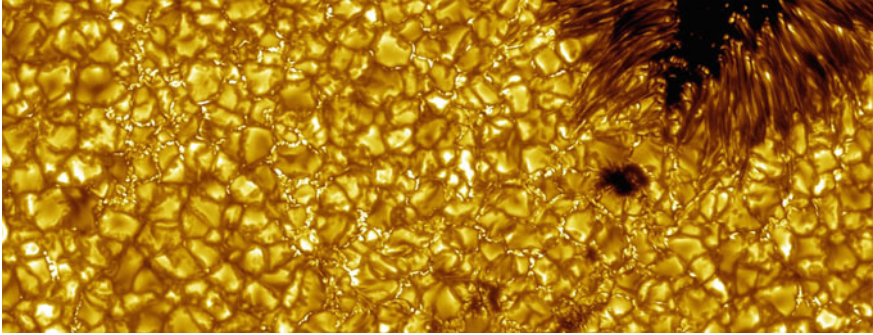


Fig. 2.3 Granulation on the solar surface, observed at high resolution with the Swedish 1-m telescope, at La Palma. A sunspot is visible in the *top-right corner*—its dark centre, known as the umbra, is surrounded by a lighter region known as the penumbra. Convection cells are visible on the photosphere surrounding the spot. Image credit: Vasco Henriques, <http://www.isf.astro.su.se/gallery/images/2010/> (link valid as of March 2015)

The vertical motions of convection produce RV variations of the order of around $2 \text{ km} \cdot \text{s}^{-1}$. Since there are about 1 million granules on the visible hemisphere of the Sun at any time, the global RV variations can be thought of as arising from fluctuations in the number of granules present. The fluctuations obey Poisson statistics, so they are on the order of the square root of the number of granules, reducing the observed RV flicker on the granulation timescale from $2 \text{ km} \cdot \text{s}^{-1}$ down to $2 \text{ m} \cdot \text{s}^{-1}$ (Lindgren and Dravins 2003). The first evidence of the such RV variations were observed by Labonte et al. (1981) and Kuhn (1983) on the Sun. Several years later, Kjeldsen et al. (1999) reported on the first clear evidence of periodic fluctuations due to granulation in a star other than the Sun, α Cen A.

We can go back to the RV observations of μ Arae, shown in Fig. 2.1 to identify its granulation signature. In panels (a) and (b), we can see variations over a longer timescale than that of the p-mode oscillations. An inspection of the periodogram in Fig. 2.2 reveals peaks close 1 and 2 h, which can be attributed to granulation (although in this particular case, these peaks may be aliases of a longer 8-h cycle that can be seen in plots of the full 8 nights of data, presented in Bouchy et al. 2005).

As for p-modes, adapting our observing strategy to mitigate their effect on RV measurements also works for granulation. Taking several RV measurements on each night observed (generally 2 to 3 measurements) spaced by about 2 h significantly reduces the RV effects of granulation (Dumusque et al. 2010).

2.1.4 Days and Longer: Gravitational Redshift

Photons escaping from the photosphere are slowed down by the strong gravitational potential of the star; the photons become redshifted, causing the centres of the spectral

lines to shift. In the case of the Sun, this results in a shift in RV of order $600 \text{ m} \cdot \text{s}^{-1}$ (Lindgren and Dravins 2003). The magnitude of this shift depends on the stellar radius, and Cegla et al. (2012) calculated that a change of 0.01 % in the radius of the Sun would induce a shift of about $6 \text{ cm} \cdot \text{s}^{-1}$ in RV. This is enough to mimic or mask the orbital reflex motion of the Earth in our solar system if the radius fluctuations are taking place on a long enough timescale. Cegla et al. (2012) found that fluctuations occurring over 10 days or longer became significant. This means that we do not have to worry about the effect of p-modes; however, changes in the granulation pattern on the stellar surface and the Wilson depression of starspots (see Solanki 2003 and references therein) can potentially produce radius fluctuations that would yield small, but significant RV variations (see Cegla et al. 2012 and references therein). Variable gravitational redshift is not a major source of activity-induced RV variations, however.

2.1.5 *Stellar Rotation Period: Spots, Faculae and Plage Regions*

Stellar surface features such as spots and networks of faculae induce photometric and spectroscopic variations that are modulated by the rotation period of the star. These signals pose a serious challenge to the detection of exoplanets. Various decorrelation methods have been developed (see Sect. 2.2), but no simple and all-inclusive recipe has yet been found.

2.1.5.1 Sunspots and Starspots

Sunspots are seen as dark areas on the surface of the Sun (see top right corner of Fig. 2.3). Hale (1908) was the first to notice Zeeman splitting of lines produced in these dark regions and deduced that sunspots are regions of strong magnetic fields. They are indeed areas where magnetic flux loops emerge from the solar surface (Solanki 2002); the magnetic fields inhibit part of the outgoing convective heat flux, resulting in areas of reduced brightness and temperature. The spots usually appear as pairs of opposite magnetic polarity. For a detailed review of the general properties of sunspots, refer to Solanki (2003).

Observations of similar dark and magnetic structures on the surfaces of other stars have led to the concept of stellar spots. Starspots are defined as “an environment in which magneto-convective interaction significantly suppresses convective energy transport over an area large enough that a structure forms that is cool and dark relative to the surrounding photosphere” (Schrijver 2002). They are similar to sunspots in many aspects; the most notable difference is that starspots can attain huge sizes and can exist near the poles of their stars (Strassmeier 2009). In the next few paragraphs, I briefly describe the main properties of sunspots and starspots.

Many of the papers cited below are part of the Proceedings of the First Potsdam Thinkshop on Sunspots and Starspots (Strassmeier et al. 2002). I also learned much on starspots from reviews by Berdyugina (2005) and Strassmeier (2009). Thomas and Weiss (2008) is a comprehensive book on starspots and sunspots. These are all excellent sources of information to find out more about the physical properties of sunspots and starspots.

Sunspots have temperatures ranging from 600 to 1800 K less than the surrounding photosphere, and starspots have similar temperature differences ranging from 500 to 2000 K (Schrijver 2002). Since spots have lower temperatures than the rest of the stellar surface, they appear darker. We can determine their magnetic field strength and the magnetic filling factor over the whole stellar surface via Zeeman splitting of spectral lines, using high-resolution spectra; we are not yet able, however, to disentangle these two quantities (Saar 1991; see Reiners 2012 and references therein).

As spots grow and decay, they induce variations in photometry that are modulated by the star's rotation (see some example lightcurves in Fig. 2.11). As a star rotates, one half of the disc is moving towards us, while the other half is moving away; as a result, the flux emitted by the approaching half is blueshifted, while the receding half is redshifted. If the stellar surface presents no features, the Doppler shifts from both sides cancel each other out and the spectral line profile is undisturbed, as pictured in the left diagram of Fig. 2.4. A starspot coming in and out of view as the star rotates, as shown in the subsequent diagrams of Fig. 2.4, blocks some of the flux of the star, inducing an imbalance between the redshifted and blueshifted halves of the star. This produces an asymmetry in the shape of the total line profile, thus shifting its centroid by a small amount. These perturbations to the line profile translate into RV variations of the order of $1 \text{ m} \cdot \text{s}^{-1}$ for sunspots (Lagrange et al. 2011; Makarov et al. 2009);

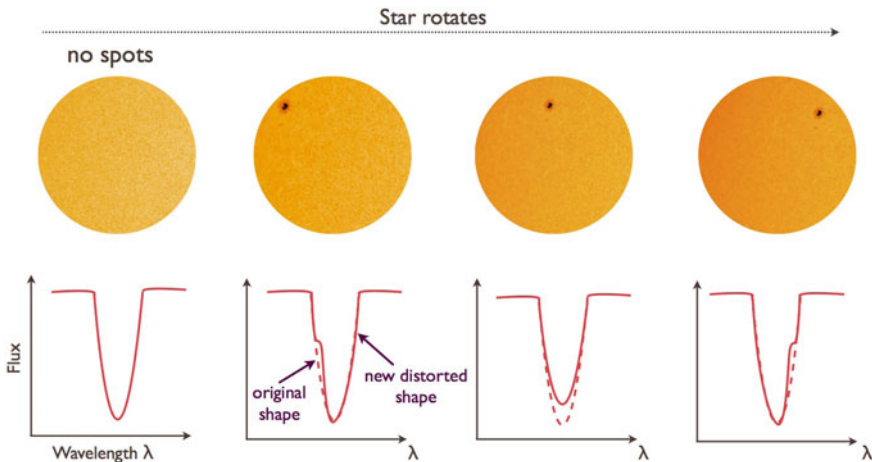


Fig. 2.4 Diagram illustrating how flux blocked by starspots on the rotating stellar disc induces asymmetries in the spectral lines, leading to variations in RV

starspot-induced RV variations can be much greater for more active, more rapidly rotating stars.

We can monitor these line-profile distortions to track the evolution of spots. This technique, commonly known as *Doppler imaging*, was first applied to the rapidly-rotating star HR 1099 by Vogt and Penrod (1983) to reconstruct a stellar surface brightness map. It was later applied to the rapidly-rotating K dwarf AB Doradus, by Donati and Collier Cameron (1997) to map the stellar magnetic flux distribution. The procedure is illustrated in Fig. 2.5, with HARPS cross-correlations functions (CCFs) of sunlight scattered from the bright asteroid Vesta (I present a detailed analysis of these observations in Chap. 5). The CCFs obtained from each observation are first stacked on top of one another to obtain a time series of line profiles, as shown in panel (a); I then compute the mean line profile shown in panel (b); finally, I subtract this mean profile from each CCF of the time series, in order to reveal asymmetries in the line profiles, as shown in panel (c). These distortions are produced by sunspot groups drifting across the solar disc. Using this technique, we can deduce the latitude of the spot groups and therefore construct maps of the stellar surface. The Doppler imaging technique works best on (fast-rotating) stars with long-lived spot groups that will remain on the stellar disc for several rotations.

Sunspots have sizes ranging from 1,500 to 20,000 km, and even the largest spots will only cover a small fraction of the solar surface ($<1\%$). The average sunspot coverage on the Sun is typically between 0.0001 and 0.1 %, depending on the phase of the solar cycle (Strassmeier 2009). It is trickier to determine the sizes of starspots as we cannot resolve their surfaces at high resolution. The amplitude of photometric variations depends on the size of a spot, or group of spots present at a given longitude, but it also depends on the contrast in brightness of the spot group, which itself depends on the temperature contrast. This is a complex issue, and many studies have been carried out to disentangle these two quantities using Doppler imaging (Catalano et al. 2002 and references therein). Doppler imaging uncovered starspots of all sizes

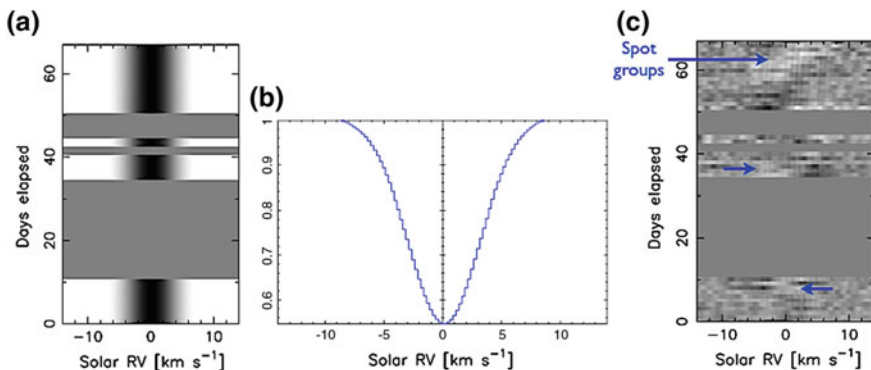


Fig. 2.5 Doppler-imaging the Sun! in three simple steps: **a** make a time series of the CCFs; **b** compute the mean line profile; **c** subtract the mean line profile from the time series to reveal line-profile distortions caused by sunspots and groups of faculae trailing across the solar disc

ranging from 0.1 up to 22 % of the stellar surface (Strassmeier 2009). There have also been observations of huge polar spots on some stars (see Schrijver 2002; Strassmeier 2009 and references therein).

Sunspots as well as small starspots live from a few days up to several weeks (Schrijver 2002; Allen 1973; Hussain 2002). In general, the lifetime of a spot is proportional to its size (Berdyugina 2005); spots decay by diffusing out into the surrounding photosphere, so spots with a relatively larger area-to-perimeter ratio should take more time to disappear (Solanki 2003; Petrovay and van Driel-Gesztelyi 1997; Robinson and Boice 1982). This has been confirmed observationally via *Kepler* data (see Helen Giles, MSci project at University of St Andrews, results to be published).

On the Sun, sunspots are always found between the latitudes of $\pm 35^\circ$; they migrate closer to the equator as the solar cycle progresses (see Sect. 2.1.6). A similar behaviour is seen on other stars, although spots can also be found at much higher latitudes. Sunspots preferentially appear at so-called active longitudes, where increased magnetic activity in a localised region causes spots to manifest repeatedly in the same region (Berdyugina and Usoskin 2003). Active longitudes have also been observed on other stars (Olah et al. 1989; Lanza et al. 2009 and others). They rotate in phase with the stellar rotation (modulo differential rotation), and could explain a persistent coherent starspot signal. Ivanov and Kharshiladze (2013) found that prominent solar active longitudes can survive for up to 20 solar rotations.

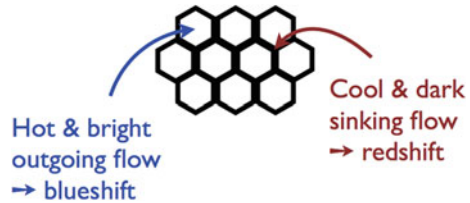
2.1.5.2 Faculae and Plage

Faculae are small bright pores on the stellar photosphere and are associated with strong magnetic fields (Spruit 1976). On the Sun, they are around 100 K hotter than the rest of the photosphere (Thomas and Weiss 2008). They are found in the intergranular lanes, and surround spots—spots are always surrounded by faculae and plage. Faculae, however, can exist on their own and are grouped together into large networks. Because they are shaped as thin flux tubes with bright walls, they are best seen near the stellar limb. Faculae have lifetimes of a couple of hours (Hirayama 1978), but groups of faculae can remain on the stellar surface for several weeks and will last for several stellar cycles. Faculae always appear before spots and will also outlive them. As we will see in Sect. 2.1.6, old and slowly-rotating Sun-like stars are dominated by faculae over starspots.

Plage regions are bright areas of the chromosphere made up of small bright points known as flocculi (see Zirin 1966 and references therein). Flocculi, or facular bright points (Soltau 1993) are surrounded by thin and dark upward moving jets known as spicules (Roberts 1945; Zirin 1966). Similarly to faculae, flocculi (and spicules) have short lifetimes of 15 to 30 min and appear brighter close to the limb (although as we get too close to the edge they become obscured by the tall spicules).

Chromospheric plage regions map closely to faculae and spots in the underlying photosphere. Plages and faculae tend to be located near sunspots, although their rela-

Fig. 2.6 Schematic representation of convection cells on the stellar surface



tionship is not yet understood (Hall 2008; Schrijver 2002). Athay (1974)³ provides further in-depth discussions on the nature of plage regions and possible relations between photospheric and chromospheric active regions (see Bumba and Ambroz 1974 in particular).

Emission lines such as Ca II H&K, H α and the Ca II triplet lines form at the level of the chromosphere, and are good indicators of plage regions (Mallik 1996; Cincunegui et al. 2007). Activity indicators based on the Ca II H&K lines are discussed further in Sect. 2.2.1.1.

The photometric effect of faculae is negligible as they are not significantly brighter than the quiet photosphere and they are evenly spread on the stellar disc; they do, however, induce a strong signature in spectroscopic observations. The strong magnetic fields present in faculae and spots act to inhibit the convection process taking place at the stellar surface. Let us think back on granulation, and take a closer look at its spatial structure. Granules can be approximated as bright hexagonal cells; they are surrounded by dark intergranular lanes, as illustrated in Fig. 2.6. The material in the intergranular lanes is cooler and therefore more compact than the hot fluid of the granules, which means that over the whole stellar disc, we see a larger proportion of hot, uprising fluid over cool, sinking material (Gray 1989). This results in a net blueshift, with a magnitude of about $200 \text{ m} \cdot \text{s}^{-1}$ on the Sun (see Meunier et al. 2010 and references therein). The presence of networks of faculae suppresses part of this blueshift.⁴ As they evolve, active regions can lead to RV variations of up to $8\text{--}10 \text{ m} \cdot \text{s}^{-1}$ for the Sun (Meunier et al. 2010), as well as the active Sun-like star CoRoT-7 (Haywood et al. 2014, see Chap. 4). Suppression of convective blueshift is thought to play a dominant role in activity-induced RV variations on Sun-like stars, particularly in the case of faculae/plage, which are thought to cover a much larger fraction of the stellar surface than spots.

2.1.5.3 Other Possible Sources of Surface Velocity Fields

As I have shown in this chapter so far, the stellar photosphere and chromosphere are bustling with all kinds of constantly evolving and moving features such as granula-

³Chromospheric fine structure: proceedings from IAU Symposium no. 56 held at Surfer's Paradise, Qld., Australia, 3–7 September 1973.

⁴Starspots also act to suppress convection, but they contribute little flux and therefore do not play a significant role in this process (see Dumusque et al. 2014 and references therein).

tion, spots, networks of faculae and plage regions. There are other phenomena that may induce RV variations, such as $\sim 50 \text{ m} \cdot \text{s}^{-1}$ horizontal inflows towards active regions recently found on the Sun (Gizon, Duvall and Larsen (2001); Gizon, Birch and Spruit (2010)). Such photospheric velocity fields may affect the RV curve (particularly when located towards the limb, as they are horizontal flows) even if they have no detectable photometric signature.

2.1.6 Decades: Magnetic Cycles

The Sun has an activity cycle of 11 years (Schwabe 1844; Hathaway 2010). Progression into the cycle towards higher activity is observed as an increase in the number of sunspots, faculae, plages and is also accompanied by a more frequent occurrence of violent events such as prominences and coronal mass ejections (see Hathaway 2010 for a detailed review). At minimum activity, sunspots are located at latitudes of $30\text{--}35^\circ$. As the cycle advances, they are found closer and closer to the equator. This results in a pattern known as the “butterfly diagram” (Maunder 1904).

In 1966, Dr Olin Wilson founded the HK Project, a survey of 1296 Sun-like stars within 50 pc of our Sun that was undertaken in an effort to characterise their activity levels and see whether other stars also displayed activity cycles similar to the Sun’s (Wilson 1968). Observations were made with the Coudé scanner attached to the 100-inch telescope at the Mount Wilson observatory. The fluxes in the Ca II H and K lines were measured, as it was already known for the Sun that the flux in these lines is correlated with the number of sunspots, i.e. an indicator of activity (Leighton 1959; Sheeley 1967—see Sect. 2.2.1.1). Wilson (1978) presented results on 91 stars after the first 11 years of observations, showing the first evidence for cyclic stellar variability.

In 1977, an improved photoelectric spectrometer was built by Dr Arthur Vaughan and placed on the 60-in. telescope, also on Mount Wilson (Vaughan et al. 1978). The activity index S was developed by Vaughan et al. (1978) in order to quantify levels of activity; I will define it further in Sect. 2.2.1.1. Values of the S -index (or the $\log R'_{\text{HK}}$, also see Sect. 2.2.1.1) for over a thousand stars were calculated and reported in Duncan et al. (1991), Baliunas et al. (1995), Henry et al. (1996), and Lockwood et al. (1997).

Baliunas et al. (1998) noticed that the majority of stars surveyed showed periodic variations with cycles of at least 7 years, and some lasting more than 30 years. A quarter of the stars displayed variability but with no apparent periodicity, while the remaining 15 % seemed to show no activity at all. The survey ran until 2003, and to this date remains the most extensive survey on stellar activity and variability. A similar and complementary project at Lowell Observatory (Arizona, USA) with the Solar-Stellar Spectrograph was initiated in 1994 (Hall et al. 2007) to record activity in Sun-like stars, and has made more than 20,000 observations since.

In parallel, it was found that as Sun-like stars get older, they rotate more slowly and their magnetic activity levels decline (Wilson 1963; Kraft 1967; Skumanich 1972,

Noyes et al. 1984). This means that young stars tend to rotate faster and be more active, and old stars like the Sun rotate more slowly and have lower activity levels.

Further studies on the variability of Sun-like stars by Radick et al. (1998) and Lockwood et al. (2007), based on the Mount Wilson and Lowell stellar samples, revealed the existence of distinct types of variability patterns. In young stars, photometric variations tend to be anti-correlated with chromospheric variations ($\log R'_{\text{HK}}$), which indicates that their surfaces are dominated by spots during phases of high activity levels. In the case of older, slowly-rotating stars such as the Sun, photometric variations are positively correlated with chromospheric variations. This means that their surfaces are dominated by faculae rather than spots. The dividing line between these two types of variability was found to be at $\log R'_{\text{HK}} = -4.7$. The Sun, with $\log R'_{\text{HK}} = -4.96$ lies just below this limit and its surface is thus faculae-dominated.

The long-term, continuous observations obtained over the last decades have given us an invaluable insight into the time-variant activity patterns of stars other than our Sun. We are still left to wonder, however, about the spatial evolution of stellar activity over these long timescales. For example, do starspots migrate across the surface in the same way that sunspots do? Sanchis-Ojeda et al. (2011) and Sanchis-Ojeda and Winn (2011) showed that it is possible to deduce the latitude of starspots occulted by planetary transits. Llama et al. (2012) successfully recovered spot locations from transit occultations in the continuous, high-precision photometry provided by the *Kepler* satellite over its 3.5-year lifetime. They carried out simulations of magnetic cycles for a range of cycle durations and found that it is possible to track the migration of spots on active stars with short activity cycles; with a longer dataset, they would be able to characterise spot-belts on Sun-like stars. A couple of simulated “butterfly diagrams” with different activity levels are shown in Fig. 2.7.

Stellar magnetic cycles can produce significant RV variations, in some cases of up to $25 \text{ m} \cdot \text{s}^{-1}$ (Lovis et al. 2011). So far, we have been searching mostly for short-period planets ($P < 50$ days). A few large RV programs with HARPS and HIRES have been running for 5–10 years (including Lovis et al. 2011; Marcy et al. 2014). They are only just beginning to catch glimpses of magnetic cycles in RV observations. In their recent detection of an Earth-mass planet with a 3-day orbit around α Centauri

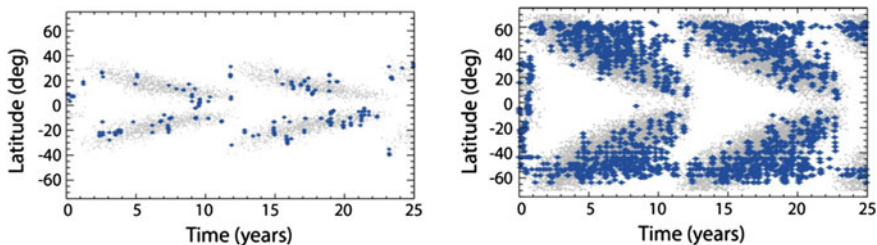


Fig. 2.7 Simulated “butterfly diagrams” for stars with an 11-year activity cycle like the Sun, with low and high activity levels, respectively. The *blue dots* show spots that have been recovered through bumps in the transit lightcurve, while the small *grey dots* represent the input butterfly pattern, for reference. These plots were made by Dr Joe Llama, based on work from Llama et al. (2012)

B, from the analysis of over 3 years of data, Dumusque et al. (2012) found that the long-term activity-induced RV variations followed the variations in $\log R'_{\text{HK}}$. They were therefore able to model the RV variations assuming a linear relationship with $\log R'_{\text{HK}}$. This may not work as well if the planet's orbital period is comparable to the magnetic cycle, however, and as we begin to look for Jupiters and Saturns with orbital periods comparable to magnetic activity cycle durations, this will become a growing concern.

2.1.7 Timescales: Summary

The surface of a star is constantly bustling with magnetic activity, which leads to a plethora of RV perturbations. On the shortest timescales (oscillations, granulation), we can average out most of the effects on RV by adapting our observing strategy. On timescales of the order of decades, assuming a linear relationship between long-term activity RV variations and $\log R'_{\text{HK}}$ variations will work as a first approximation, although as we begin to look for long-period planets we are going to require more effective methods and proxies.

The most complex activity-induced RV variations, which cause the most trouble in today's RV exoplanet surveys arise from processes taking place on the stellar rotation timescale. Strongly magnetised photospheric features such as starspots and networks of faculae (as well as chromospheric plage regions) inhibit convective motions occurring just below the stellar surface, thus suppressing part of the blueshift naturally resulting from granulation. This effect can lead to variations in RV of up to $10 \text{ m} \cdot \text{s}^{-1}$ (Meunier et al. 2010; Haywood et al. 2014). In addition, starspots coming in and out of view as the star rotates induce an imbalance between the redshifted and blueshifted halves of the star which translates into an RV modulation of the order of $1 \text{ m} \cdot \text{s}^{-1}$ (Lagrange et al. 2011; Makarov et al. 2009). There may even be other processes at play which induce significant RV variations (Haywood et al. 2014), such as horizontal flows toward active regions (Gizon et al. 2001, 2010) or other unknown processes, whose impact on RV variations will require further investigation.

Identifying informative and reliable proxies for activity-driven RV variations has become crucial for exoplanet detection and characterisation. In the next section, I outline the various proxies and activity decorrelation techniques that have been developed for RV planet searches so far.

2.2 Existing Treatments for Activity-Induced RV Variations

This section provides a detailed summary of the analysis techniques developed to identify planetary signals in the presence of stellar activity. The methods of harmonic decomposition, pre-whitening and nightly offsets were initially developed to determine the mass of transiting super-Earth CoRoT-7b, so if you wish to place them in

a more “historical” context, you can read the introduction on CoRoT-7 in Chap. 4, Sect. 4.1.1 in parallel.

2.2.1 Spectroscopic Activity Indicators

The following indicators, derived from the same stellar spectra used to measure the stellar RV, are affected by stellar activity only, so any variations present in RV observations but not seen in these indicators may point to a planetary signal.

2.2.1.1 Activity Indicators Based on Ca II H & K Line Fluxes

The S -index was first used by Vaughan et al. (1978). In his review on stellar chromospheric activity, Hall (2008) defines it as “a dimensionless ratio of the emission in the line cores [of Ca II H & K] to that in two nearby continuum bandpasses on either side of the H and K lines”. The S -index can therefore be expressed as:

$$S = \alpha \frac{\Psi_H + \Psi_K}{\Psi_V + \Psi_R}, \quad (2.1)$$

where Ψ_H and Ψ_K refer to the fluxes in the cores of the H and K lines respectively, and Ψ_V and Ψ_R refer to the fluxes in the bands on the violet and red sides of the H and K lines. The term α is a normalisation factor. The amount of flux measured in the reference passes, however, depends on spectral type so the S index cannot be used to compare stars of different colours. The S -index also varies when applied to measurements taken with different instruments, since the level of transmission of the bandpasses depends intrinsically on the instrumentation used. Middelkoop (1982) was the first to apply a correction term to the S -index in order to overcome its color dependence.

The R'_{HK} index was introduced by Noyes et al. (1984) in an effort to propose an activity index independent on spectral type and instrument design. Hall (2008) defines it as “the fraction of a star’s bolometric luminosity radiated as chromospheric H and K emission”. This is expressed in mathematical terms as (Martínez-Arnáiz et al. 2010):

$$R'_{HK} = \frac{\Psi'_H + \Psi'_K}{\sigma T_{\text{eff}}^4}, \quad (2.2)$$

where σ denotes the Stefan–Boltzmann constant and T_{eff} is the effective temperature of the star. The primes on the fluxes Ψ are to show that the chromospheric contribution of the reference star has been subtracted. Note that there Ψ' values in this context are also in the form of fluxes measured at the stellar surface, rather than those received by the observer, to be consistent with the use of σT_{eff}^4 . The R'_{HK} index is widely used, usually in logarithmic units.

2.2.1.2 Indicators Derived from the Cross-Correlation Function

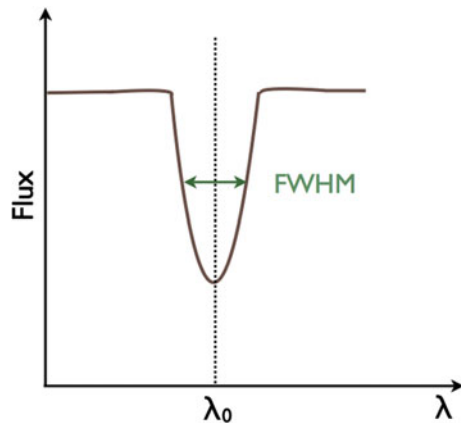
As I described in the previous chapter, in order to measure the RV of a star all the lines of a spectrum are combined together to produce a mean line profile known as the cross-correlation function (CCF). Its shape reflects the shape of all the lines in the spectrum, which are affected by physical processes taking place in the stellar atmosphere, where these lines form. Here I present two measures of the shape of the CCF, that have been used in previous studies to identify activity-induced signals in RV data.

Full width at half-maximum (FWHM) The full width at half-maximum of the CCF, or FWHM is shown in Fig. 2.8. The FWHM is determined by the stellar rotation rate, i.e. the $v \sin i$ of the star (Desort et al. 2007). Since younger, fast rotating stars tend to be more active, it ensues that the FWHM gives a general indication of the levels of magnetic activity of a star. The FWHM also incorporates the intrinsic width of the line due to thermal and turbulent motions in the stellar photosphere.

The FWHM changes as a spot of facular region crosses the stellar disc, in order to conserve the area enclosed by the line profile (see Fig. 2.4). RV perturbations arising from the flux blocked by starspots on a rotating star are therefore correlated with variations in the FWHM. This indicator has been used by a number of studies, including Queloz et al. (2009), Hatzes et al. (2010) and Lanza et al. (2010) in the case of CoRoT-7 (see Chap. 4, Sect. 4.1.1) to identify activity-related signals.

Bisector of the cross-correlation function (BIS) A more sophisticated measure is the bisector of the CCF (see Fig. 2.9). It is defined as a measure of the general asymmetry of the lines of a spectrum (Voigt 1956), and was first used for exoplanet detection by Queloz et al. (2001). A more rigorous definition of the bisector, given by Perryman (2011) is: “the locus of median points midway between equal intensities on either side of a spectral line, thereby dividing it into two halves of equal equivalent width”. For a line profile with a perfect Gaussian shape, this would be a straight

Fig. 2.8 The full width at half-maximum of the cross-correlation function



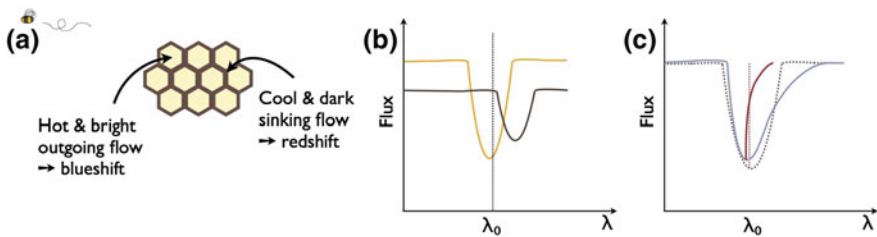


Fig. 2.9 How the shape of the line bisector is affected by surface granulation. *Panel a* Schematic representation of granulation pattern. *Panel b* Line profiles resulting from light emitted by the bright granular regions (top, yellow line) and dark intergranular regions (bottom, brown line). *Panel c* Effective line profile (blue), with its “C”-shaped line bisector (red); the undisturbed profile and its bisector are drawn in dotted lines. This figure was inspired from a similar figure in Dravins et al. (1981)

vertical line going through the middle of the line profile (dotted lines in Fig. 2.9c). However, the net blueshift produced by granulation on the stellar surface (explained back in Sect. 2.1.5.2) results in a bisector curved towards the top (see Fig. 2.9c). The granulation pattern is made of dark regions surrounding bright granules (panel (a); see Sect. 2.1.3). The bright upflowing granules produce the blueshifted line profile shown in yellow in panel (b), while the dark sinking intergranular flow leads to the redshifted line with a lower intensity, shown in brown on panel (b). The total line profile is the sum of these two profiles, as pictured in blue in panel (c). It is asymmetric, and its bisector (full red line) is curved at the top. Active regions that reduce this net blueshift will thus produce small distortions in the bisector. Many quantities have been defined in relation to the bisector, such as the bisector velocity span (Toner and Gray 1988), the curvature of the line bisector (Hatzes 1996), and the bisector inverse slope (Queloz et al. 2001); see Figueira et al. (2013) and references therein for more detail.

Desort et al. (2007) found that the FWHM, the BIS and photometric variations do not give enough information for slowly rotating, Sun-like stars (low $v \sin i$) to disentangle stellar activity signatures from the orbits of super-Earth-mass planets (see also Chap. 5, Section 5.4.2).

2.2.2 Nightly Offsets Method

This technique is very effective for short-period planets observed 2 to 3 times each night. It was successfully applied to the CoRoT-7 and Kepler-78 systems (Hatzes et al. 2010, 2011; Pepe et al. 2013; see Chap. 4).

Activity-related signals change on relatively long timescales (of the order of P_{rot}), whereas the planet’s orbital period will be of a few hours (up to 1–2 days). In such a case, it is reasonable to assume that, on a given night, the rotation-modulated stellar activity contribution to the RV signal is roughly constant, and all the variations

occurring over the span of a few hours are caused by the orbital reflex motion of the planet. This will work well for stars with low granulation “flicker” (see Sect. 2.3.2.3 which introduces the F8 statistic, a good measure of this noise source).

We can fit a linear function of the form:

$$m_i = A \cos(\omega t_i) + B \sin(\omega t_i) + C_j, \quad (2.3)$$

where A and B give the amplitude and phase of the RV signal, and there is an offset C_j for each night which represents the offset produced by the slowly varying activity modulation. The best-fit parameters can be determined via an optimal scaling procedure as follows. First, C_j is calculated for each night by taking the variance-weighted average of the data y_i in each single night:

$$\hat{C}_j = \frac{\sum_{i=1}^{n_j} y_{ij} w_{ij}}{\sum_{i=1}^{n_j} w_{ij}}. \quad (2.4)$$

The subscript j refers to each night and goes from 1 to the total number of nights, whereas the subscript i refers to each individual data point in each night and goes up to the number of points in each night (n_j). w_i are the inverse variance weights defined as:

$$w_i = \frac{1}{\sigma_i^2}, \quad (2.5)$$

where σ_i is the error associated with the data y_i .

The constant parameters A and B are found by performing the following summations over the whole dataset:

$$\hat{A} = \frac{\sum_{ij} [y_{ij} - \hat{C}_j - \hat{B} \sin(\omega t_{ij})] \cos(\omega t_{ij}) w_{ij}}{\sum_{ij} \cos^2(\omega t_{ij}) w_{ij}}, \quad (2.6)$$

and

$$\hat{B} = \frac{\sum_{ij} [y_{ij} - \hat{C}_j - \hat{A} \cos(\omega t_{ij})] \sin(\omega t_{ij}) w_{ij}}{\sum_{ij} \sin^2(\omega t_{ij}) w_{ij}}. \quad (2.7)$$

An iteration is then carried out until A and B both converge. For further detail on iterative optimal scaling, the reader may refer to Collier Cameron et al. (2006) or Keith Horne’s *Ways of Our Errors*.⁵

⁵Unpublished as of August 2015 but available online at: <http://star-www.st-and.ac.uk/~kdh1/ada/woe/woe.pdf>.

2.2.3 Harmonic Decomposition

As shown by Jeffers et al. (2009), any starspot configuration can be modelled by a series of harmonics of P_{rot} containing only the first three or four Fourier terms.⁶ Subtracting this model from the data will help reveal signals that do not originate from the star's activity. Harmonic decomposition is based on three parameters: the stellar rotation period, the number of harmonics and the coherence time. The rotation period can be determined via Lomb–Scargle or autocorrelation techniques, which I describe later in Sects. 2.3.2.1 and 2.3.2.2.

Harmonic decomposition can be implemented by fitting a Fourier series of the form:

$$m_i = m_0 + \sum_{k=1}^l [C_k \cos(k \omega t_i) + S_k \sin(k \omega t_i)], \quad (2.8)$$

where the number of desired harmonics is given by l and m_0 is a constant. The best fit can be determined via an iterative optimal scaling procedure akin to that presented in Sect. 2.2.2.

In this case, the inverse variance weights are given by:

$$w_i = \frac{\mathcal{G}(t - t_i)}{\sigma_i^2}, \quad (2.9)$$

where \mathcal{G} is a Gaussian function defined as:

$$\mathcal{G}(t - t_i) = \exp\left[-\frac{1}{2}\left(\frac{t - t_i}{\tau}\right)^2\right]. \quad (2.10)$$

τ is the coherence time. It governs the time interval over which each data point at time t_i retains its importance. τ is normally chosen to be slightly less than the rotation period of the star, so that it is short enough to filter out the slow varying signals (due to activity—starspots usually have lifetimes of about one rotation period or longer), but not so much that it will destroy short period signals.

This technique was applied to CoRoT-7 using the first three harmonics (Queloz et al. 2009; Hatzes et al. 2010), and up to the first six harmonics (Ferraz-Mello et al. 2011). It was found that the activity signal can be reproduced nearly perfectly using only the first three (Queloz et al. 2009), since for higher harmonics the amplitude of the signal becomes negligible.

⁶As a side note, this also means that we cannot reconstruct a map of the stellar surface solely based on its photometric variations!

2.2.4 Pre-whitening

A Fourier analysis is carried out to find the strongest period in the signal, and a sinusoidal fit with this period is subtracted from the data. We repeat this until the noise level is reached. This is a quick way to uncover the strongest periods present in the signal and to compose a periodogram. It is analogous to the CLEAN method derived by Högbom (1974) and Roberts et al. (1987). See also Queloz et al. (2009) and Hatzes et al. (2010).

2.2.5 The FF' Method

Aigrain et al. (2012) found that RV variations induced by starspots are well reproduced by a model consisting of the product of the photometric flux F and its first time derivative F' . It is assumed that the spots are small and limb-darkening is ignored. Spots influence the stellar RV by suppressing the photospheric surface brightness at the local rotational Doppler shift of the spot. Also, in areas of high magnetic field such as faculae, which on the Sun are often associated with spot groups, the convective flow is inhibited, leading to an attenuation of the convective blueshift (see Sect. 2.1.5.2). This effect is thought to be the dominant contribution to the total RV signal in the Sun (Meunier, Desort and Lagrange 2010).

As shown in Fig. 2.10, the RV perturbation ΔRV_{rot} to the star's RV incurred by the presence of spots on the rotating photosphere varies with both the flux deficit of the spot (F) and the line-of-sight velocity; F varies with foreshortening, so it has a cos phase, while the line-of-sight velocity varies with a sin phase (so it is proportional to F'). As derived in Aigrain et al. (2012), the RV perturbation due to a spot crossing the disc can be expressed as follows:

$$\Delta RV_{\text{rot}}(t) = -\frac{\dot{\Psi}(t)}{\Psi_0} \left[1 - \frac{\Psi(t)}{\Psi_0} \right] \frac{R_\star}{f}, \quad (2.11)$$

where $\Psi(t)$ is the observed stellar flux, Ψ_0 is the stellar flux for a non-spotted photosphere and $\dot{\Psi}(t)$ is the first time derivative of $\Psi(t)$. R_\star is the stellar radius. The parameter f represents the drop in flux produced by a spot at the centre of the stellar disc, and can be approximated as:



Fig. 2.10 The FF' method for a spot crossing the stellar disc. The RV variations induced by flux blocking (ΔRV_{rot}) and suppression of the convective blueshift (ΔRV_{conv}) are proportional to $F dF/dt$ and F^2 , respectively

$$f \approx \frac{\Psi_0 - \Phi_{\min}}{\Psi_0}, \quad (2.12)$$

where Φ_{\min} is the minimum observed flux, i.e. the stellar flux at maximum spot visibility.

The effect of the suppression of convective blueshift on the star's RV produced by starspots and magnetised areas surrounding them, written as ΔRV_{conv} , is shown in Fig. 2.10. ΔRV_{conv} varies with foreshortening and the angle between the convective velocity vector and the line of sight. Both vary with the flux, so ΔRV_{conv} depends on F^2 :

$$\Delta RV_{\text{conv}}(t) = \left[1 - \frac{\Psi(t)}{\Psi_0} \right]^2 \frac{\delta V_c \kappa}{f}, \quad (2.13)$$

where δV_c is the difference between the convective blueshift in the unspotted photosphere and that within the magnetised area, and κ is the ratio of this area to the spot surface (Aigrain et al. 2012). The two RV basis functions are pictured in Fig. 2.10.

This method does not depend on the period of rotation of the star, nor does it rely on complicated spot models. Aigrain et al. (2012) report on tests on HD 189733 that show it successfully reproduces previous results based on more complex models (Lanza et al. 2011). They also tested it on 600 *Kepler* targets and obtained promising results, given that the FF' method is very easy and quick to implement and could thus be applied to large datasets.

The FF' method is likely to provide an incomplete representation of activity-induced RV variations, however (Haywood et al. 2014—see Chap. 4, Sect. 4.1). The FF' method does not consider the broad-band photometric effect of faculae that are not physically associated with starspots; Aigrain et al. (2012) assume that their effect on ΔRV_{rot} is quite small as they tend to have low photometric contrast. Indeed, according to Lockwood et al. (2007), faculae become less important (relative to spots) in stars more active than the Sun (see Sect. 2.1.6). Faculae do, however, have a significant impact on the suppression of convective blueshift (Meunier et al. 2010); indeed we find that this effect dominates the total RV contribution induced by stellar activity (see Sect. 4.1.5.7). There are other phenomena that the FF' method does not account for, such as $\sim 50 \text{ ms}^{-1}$ inflows towards active regions recently found on the Sun (Gizon et al. 2001, 2010—see Sect. 2.1.5.3). Such photospheric velocity fields may affect the RV curve even if they have no detectable photometric signature. In addition, some longitudinal spot distributions have almost no photometric signature, so the FF' method would not account for them.

2.2.6 Existing Methods: Summary

The planet masses determined via all these methods should all agree, though the RMS scatter in the residuals may differ depending on how good the assumptions are. This reflects the fact that planet mass determinations are intimately tied to the methods

that we use to model activity-induced RV variations. It is therefore crucial that we design effective decorrelation techniques (see Chap. 4) and better proxies for activity signals (see Chap. 5). In the meantime, we can minimise the problem by selecting stars that are less likely to show activity-induced RV variations; this is the focus of the next section of this chapter.

2.3 RV Target Selection Based on Photometric Variability

Since we do not yet know how to fully and reliably model all activity-induced RV variations, it is essential that we carefully pick stars for RV follow-up. Otherwise we may unknowingly choose a star with a rotation period that matches the orbital period of the planet, for example, and end up wasting huge amounts of telescope time for an imprecise, potentially even inaccurate planet mass determination.

Stars that have been observed by the high-precision photometry CoRoT and *Kepler* missions are ideally suited for potential RV follow-up, as we can learn a lot about their magnetic behaviour from their lightcurves.

The following question springs to mind: how do we define a magnetically “manageable” star for RV follow-up? This not only depends on the amplitude and frequency structure of activity variability; it is also tied with the mass and orbital period of the planet, and the decorrelation methods that we have developed to date.

For example, it is relatively easy to determine the mass of a super-Earth with a very short orbital period (typically less than 1 day), even if the host star is very active; the orbital and stellar rotation periods will be so different that we can take several observations per night and assume that all the variations produced within each night are solely due to the planet’s orbital motion (see Sect. 2.2.2).

As a member of the Target Selection Tiger Team of the HARPS-N Guaranteed Time Observations collaboration, I was led to define magnetic manageability criteria to help us identify suitable *Kepler* candidates for HARPS-N RV follow-up (summer season of 2014).

2.3.1 Preliminary Target Selection Criteria

Before subjecting *Kepler* candidates to activity-related triage, a preliminary selection (from a pool of 600 available targets) was done by other members of the HARPS-N team. It includes the following criteria:

1. Target brightness: the majority of *Kepler* stars are too faint for ground-based RV follow up. This criterion was embedded in an estimation of the RV precision that would be achieved with the HARPS-N instrument. In this particular aspect, HARPS-N is a twin of HARPS, so we can use a relatively simple formula

determined by Bonfils et al. (2013). As a rule of thumb, stars should have a magnitude less than $V \approx 13$ mag.

2. Time required for a (3- or) 6-sigma detection: this can be calculated from the expected RV semi-amplitude of the planet candidate, which can itself be derived by assuming a bulk density (either a fixed value e.g. $\rho = 3 \text{ g} \cdot \text{cm}^{-3}$, or a radius-dependent value determined from mass-radius relations such as those derived by Weiss and Marcy 2014).
3. Number of planet candidates in the system; scientific interest related to each individual candidate (what is the scientific goal of this study: are we trying to populate the mass-radius diagram at a given radius/mass range? Are we trying to find other rocky mini-Neptunes like Kepler-10c?).
4. Observability: depending on how many months/years our survey is likely to last, determine the longest orbital periods it is reasonable to consider.
5. Asteroseismology information: this should be available if the target has been observed at short-cadence by *Kepler* or CoRoT. It will provide robust stellar parameters, which are essential to obtain a precise planet mass determination.
6. Previous follow-up: check the literature to see if this system has already been followed-up, and if this is the case, to assess whether additional RV measurements would be useful (eg., to determine the mass to a better precision, or to look for additional companions).

2.3.2 Generalised Lomb–Scargle Periodograms and Autocorrelation Functions

118 *Kepler* candidates survived these cuts. In order to identify activity selection criteria for these candidates, I computed Lomb–Scargle periodograms and autocorrelation functions (Lomb 1976; Scargle 1982; Edelson and Krolik 1988; Zechmeister and Kürster 2009) for the *Kepler* lightcurves of each star. I concatenated the lightcurves all the quarters together by dividing by the inverse variance weighted mean flux level for each quarter. This procedure is approximate but works well, as confirmed by visual inspection of a few lightcurves (see Fig. 2.11).

In the next two sections, I outline the concepts and main equations of the Lomb–Scargle periodogram and autocorrelation techniques.

2.3.2.1 Generalised Lomb–Scargle Periodogram

A natural first step as a planet hunter is to make a periodogram of the data, to get a first feel for what is in it. Most activity-induced signals will show some quasi-periodicity with a recurrence timescale related to the stellar rotation period, P_{rot} and/or its harmonics. The rotation of the star modulates both the lightcurve and RV curve.

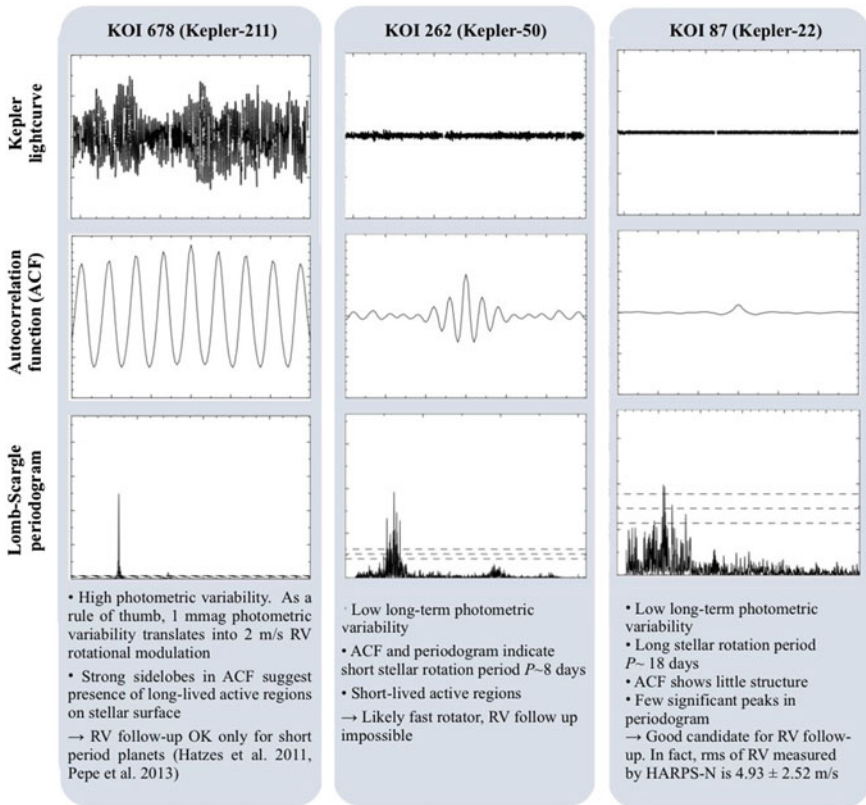


Fig. 2.11 Revealing the temporal behaviour of *Kepler* main sequence stars, through autocorrelation (time lag versus power) and Lomb–Scargle periodogram (frequency versus power) analyses of high-precision *Kepler* photometry, spanning all quarters of data. Note that all three lightcurve plots are on the same scale, ranging from -3 to $+3$ mmag. The plots were made using Andrew Collier Cameron’s *dcfpgm.f* code

The following method is based on the techniques proposed by Lomb (1976), Scargle (1982) and Zechmeister and Kürster (2009). We can fit a sinusoid to our dataset:

$$m_i = A \cos(\omega t_i) + B \sin(\omega t_i) + C, \quad (2.14)$$

where A and B are the amplitudes of the signal, C is an offset from zero, m_i is the fit to the photometric or RV data y_i at time t_i and $\omega = \frac{2\pi}{P_{\text{rot}}}$ is the angular frequency associated with P_{rot} .

The parameters A , B and C are calculated using iterative optimal scaling (also known as weighted least squares):

$$\hat{A} = \frac{\sum_i [y_i - \hat{C} - \hat{B} \sin(\omega t_i)] \cos(\omega t_i) w_i}{\sum_i \cos^2(\omega t_i) w_i}, \quad (2.15)$$

$$\hat{B} = \frac{\sum_i [y_i - \hat{C} - \hat{A} \cos(\omega t_i)] \sin(\omega t_i) w_i}{\sum_i \sin^2(\omega t_i) w_i}, \quad (2.16)$$

and

$$\hat{C} = \frac{\sum_i [y_i - \hat{B} \sin(\omega t_i) - \hat{A} \cos(\omega t_i)] w_i}{\sum_i w_i}. \quad (2.17)$$

The inverse-variance weights, w_i are defined in Eq. 2.5. The three parameters are summed over all data. The operation is repeated until a convergence threshold is met, for example when the change in each parameter is less than a given fraction of their associated uncertainty.

The right frequency is found by optimising the chi square (χ^2) on a grid of frequencies. The χ^2 is defined as:

$$\chi^2 = \sum_i [(y_i - m_i)^2 w_i]. \quad (2.18)$$

The range of frequencies to be searched starts at the sidelobe frequency ($d\omega$) up to the Nyquist frequency (ω_{nyq}) at intervals given by the sidelobe frequency of the dataset. These two quantities are given by:

$$d\omega = \frac{2\pi}{t_{\text{tot}}} \quad (2.19)$$

and

$$\omega_{\text{nyq}} = \frac{n\pi}{t_{\text{tot}}}, \quad (2.20)$$

where n is the number of points in the dataset, and t_{tot} is the total span of the observations. Care should be taken to have both frequencies in the same units ($\text{rad} \cdot \text{s}^{-1}$ or $\text{deg} \cdot \text{sec}^{-1}$).

Zechmeister and Kürster (2009) provide slightly different equations that are very easy to implement and quick to compute. We can also calculate false alarm probability levels for each signal. They are a measure of how likely it is for a signal with a given power to be caused purely by noise. Refer to Cumming (2004) and Collier Cameron et al. (2009) for a recipe on how to implement them.

2.3.2.2 Autocorrelation Function

Another way to determine the stellar rotation period is to compute the autocorrelation function of the data (Edelson and Krolik 1988). This technique provides us with

much more than just the period of the main signals in the data; an autocorrelation function is a star's activity identity card. The autocorrelation function conveys the same information as the Lomb–Scargle periodogram: with one glance at it we can tell the rotation period, whether the star has spots, how long they live for, how fast they decay, if there are many active regions, etc. The concept is the following: we take two copies of our dataset and shift them against each other by a small time interval τ at each step. The discrete autocorrelation of a dataset y (observation times t , uncertainties σ) is equal to (Edelson and Krolik 1988):

$$k_{i,j} = \frac{(y_i - \hat{y})(y_j - \hat{y})}{\sqrt{\sigma_i^2 \sigma_j^2}}, \quad (2.21)$$

where \hat{y} is the inverse-variance weighted average of the dataset, defined as:

$$\hat{y} = \frac{\sum_{i=1}^n y_i / \sigma_i^2}{\sum_{i=1}^n 1 / \sigma_i^2}. \quad (2.22)$$

The autocorrelation function can be normalised to 1 by dividing by its maximum. Each pair of points i, j is associated with the time lag:

$$\Delta t_{i,j} = t_j - t_i. \quad (2.23)$$

For best results, the coherence length τ should be at least a few times longer than the spacing of the data, so that the autocorrelation looks smooth, but short-period signals longer than τ are still resolved.

For faster computation, only the positive (or negative) side of the autocorrelation function can be calculated and then simply mirrored onto the opposite side for plotting. The main recurrence timescale (in our case, the stellar rotation period) is the time lag of the centre of the first sidelobe of the autocorrelation function. A parabola can be fitted to this sidelobe in order to determine a more precise value, for example via iterative optimal scaling.⁷

2.3.2.3 Application to *Kepler* Lightcurves

Although I did implement my own versions of these techniques, for this target selection work I used Andrew Collier Cameron's code for discrete correlation functions & periodograms (dcfpgm.f), which I adapted for my own purposes. Figure 2.11 shows

⁷See Advanced Data Analysis course by Keith Horne online at <http://star-www.st-and.ac.uk/~kdh1/ada/ada.html> (link valid as of March 2015). The method of optimal scaling is explained in his notes from Lecture 5. His draft textbook "*The Ways of Our Errors*" is a gold mine to the astronomer looking for optimal data analysis methods.

lightcurves, Lomb–Scargle periodograms and autocorrelation functions for three example stars, with a short description of what we can learn about the behaviour of each star based on this information. In addition, I retrieved the following information:

- Two measures of the stellar rotation period—taken to be the strongest periodic signal identified in the Lomb–Scargle periodogram, and the time lag between the two main peaks of the autocorrelation function.
- The root mean scatter (RMS) of the *Kepler* lightcurves, obtained after removing points lying more than 5-sigma beyond average in order to remove any transits.
- The mean photometric error, σ_{av} , defined as the mean relative error in the *Kepler* photometry.
- The ratio between the amplitude of the main peak of the autocorrelation function (at zero time-lag) and the next highest peak: it tells us about the lifespans of active regions on the stellar surface.
- The F_8 statistic defined by Bastien et al. (2013), in units of parts per thousand (ppt). It corresponds to the RMS of the lightcurve over an 8-h timescale. It is computed by taking the RMS scatter in the photometry residuals after applying a boxcar filter of width 8 h. This scatter is caused by granulation and is known as the “8-h flicker”. Faint stars will naturally display more variability in F_8 , which we correct for by applying the relation used by Bastien et al. (2013), based on the *Kepler* magnitude V_{kepler} of the star (available in the *Kepler* input catalogue):

$$\log_{10} F_8 = -0.03910 - 0.67187 V_{kepler} + 0.06839 V_{kepler}^2 - 0.001755 V_{kepler}^3 \quad (2.24)$$

- $\log g$: I deduced this value from the F_8 statistic, using the relationship established by Bastien et al. (2013):

$$\log_{10} g = 1.15136 - 3.59637 \log_{10}(F_8) - 1.40002 \log_{10}(F_8)^2 - 0.22993 \log_{10}(F_8)^3 \quad (2.25)$$

It is useful to check the value of the $\log g$ as it gives an indication of whether the star is on the main sequence or if it is a giant or sub-giant star. Giants and sub-giants have lower surface gravity, bigger atmospheric scale heights, and hence fewer granules. The uncertainty in the number of granules on the stellar surface at any time is proportional to the square root of the number of granules (see Sect. 2.1.3), so the fractional uncertainty, and hence the noise (quantified in the F_8 statistic), goes up when there are fewer granules (Lindgren and Dravins 2003).

The plots in Fig. 2.12 illustrate the general behaviour of all 118 stars as a sample.

Stellar rotation periods The rotation periods obtained via both methods are plotted against each other in panel (a) of Fig. 2.12. They are in good agreement overall. In a few cases, especially at long periods, the period identified via Lomb–Scargle is twice as long as that of the autocorrelation. Period halving is a common problem at times when there are active regions on opposing hemispheres of the star. In such cases the autocorrelation sidelobes often alternate in amplitude, making it easier to

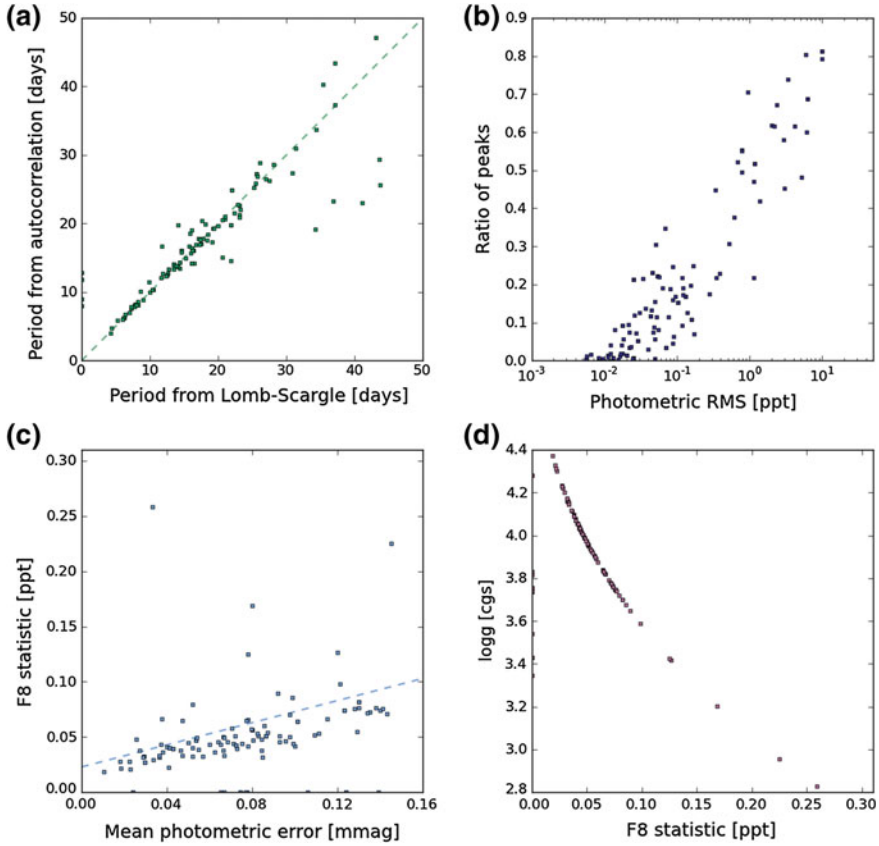


Fig. 2.12 Photometric variability characteristics of our stars as a sample. *Panel a* periods obtained through both methods plotted against one another; *panel b* Main-peak-to-first-sidelobe of autocorrelation function ratio, as a function of photometric RMS; *panel c* F_8 statistic plotted versus mean photometric error, σ_{av} ; *panel d* $\log g$ values derived from the F_8 statistic. (The stars with zero Lomb–Scargle period or zero F_8 statistic are errors arising from the code, and further investigation would be required to solve this.)

identify the true period. I decided to use the stellar rotation period obtained from the autocorrelation method.

Care should be taken, however, mainly for two reasons:

- The majority of the stars in our sample show very little photometric variations; many stars display photometric RMS of order 0.1 or even 0.01 parts per thousand (ppt), as seen in panel (b) in Fig. 2.12. This means that it can be difficult to measure the rotation period reliably, even through the autocorrelation method which will exhibit weak sidelobe amplitudes.
- The lightcurves were reduced with *Kepler*'s PDC-MAP pipeline (Stumpe et al. 2012), which is a decorrelation method designed to remove patterns of instrumental

origin that are common to all stars in a given field of view of the *Kepler* CCD. It should not suppress signals of astrophysical origin, particularly variations due to the star’s rotation and activity on short timescales. However, the *Kepler* Data Release 21 Notes caution that the PDC-MAP lightcurves should not be used to look for periodic signals longer than 20 days, as the pipeline erases long-term trends. On the other hand, McQuillan et al. (2014) and others have shown that it is possible to obtain reliable stellar rotational periods for a large number of *Kepler* stars.

Active region lifetimes The plot in panel (b) of Fig. 2.12 shows that there is a correlation between the amplitude of the star’s photometric variations (RMS of the lightcurve) and the lifespan of active regions, which indicates that large active regions live longer. Starspots are thought to decay through diffusion, which takes place around the edge of the spots: larger spots, which have a smaller perimeter-to-area ratio will thus take longer to diffuse away (see references in Sect. 2.1.5.1).

2.3.3 Selection Criteria for “Magnetically Manageable” Stars

I settled on the following selection criteria:

1. Eliminate stars with a rotation period of less than 10 days, as we do not want to do RV follow-up on fast rotators (the cross-correlation profile would be very broad and yield a poorly-constrained RV measurement).
2. Require the RMS of the lightcurve to be less than 0.001 mag. This seemed like a reasonable threshold beyond which the star is showing a lot of modulation from starspots coming in and out of view.
3. In order to eliminate stars with anomalously high levels of granulation noise, I require:

$$\frac{(F_8 - 0.023)}{1000\sigma_{\text{av}}} < 0.5. \quad (2.26)$$

The value 0.023 mag corresponds to the flicker “floor” seen in panel (c) of Fig. 2.12; an F_8 value below this limit indicates that the star is faint enough for the photon noise to dominate photometric variations induced by granulation. A high F_8 value makes it harder to average out the RV variations caused by granulation, even if we make a couple of observations separated by two hours. Indeed, most *Kepler* targets are so faint that we need to make 1800-s (30 min) exposures, and we therefore cannot really afford to take two per night.

4. Rotational and orbital timescales: it is more difficult to disentangle the orbit of a planet if its orbital period is close to the stellar rotation P_{rot} or its first harmonics. I discarded cases where the orbital period is within 2 days of P_{rot} , $P_{\text{rot}}/2$, and $P_{\text{rot}}/3$. I chose an interval of 2 days to be on the safe side since the stellar periods may not be very accurate.

5. It is also a problem if the orbital and stellar rotation timescales are too similar. I discarded cases where the rotation period was less than twice the orbital period.
6. However, if the timescales are *very* dissimilar, we can consider more active stars, i.e. a larger RMS. For these systems we can apply the nightly offset method detailed in Sect. 2.2.2. I therefore included targets for which the stellar rotational period is at least 10 times longer than the planet's orbital period, even if the photometric RMS was greater than 0.001 mag.
7. Distinguishing main sequence stars from giants: I require all viable candidates to have a $\log g$ greater than 3.5. This cutoff value is somewhat arbitrary, and it would be interesting to delve further into this to refine this criterion. The F_8 and $\log g$ are shown plotted against each other in panel (d) of Fig. 2.12.

2.4 Concluding Note: From Photometric to Radial-Velocity Variations

The next step would be to combine some of these indicators to predict the amplitude of activity-induced RV variations we might expect. The FF' method of Aigrain et al. (2012) (explained in Sect. 2.2.5) gives a recipe for doing exactly this. It does not fully account for the effect of faculae on the suppression of convective blueshift, or effects that have no photometric signature, however, so it is likely to largely underestimate the amplitude of activity-induced RV variations (see my work on CoRoT-7 in Chap. 4 and Haywood et al. 2014).

Based on RV data for CoRoT-7, Kepler-10 and Kepler-78 (see Chap. 4), as well as the findings of Aigrain et al. (2012), we can infer a simple rule of thumb: 1 mmag of photometric RMS results in $2 \text{ m} \cdot \text{s}^{-1}$ of activity-induced RV variations. Of course, the amplitudes are not the whole story; Bastien et al. (2014) found that the Fourier components of the lightcurve provide important clues about the complexity of the activity-induced RV variations. In this perspective, decoding the temporal structure of a star's lightcurve is a natural step towards understanding stellar RV variability.

The frequency structure of stellar signals reflects the character and personality of a star. We can use it to build a model for activity-induced RV variations, as I will show in the next chapter.

References

- Aigrain S, Pont F, Zucker S (2012) *Mon Not R Astron Soc* 419:3147
- Allen C (1973) *Allen: astrophysical quantities*, 3rd edn. The Athlone Press - Google Scholar (University of London)
- Athay RG (1974) *Proceedings of the International Astronomical Union*, vol 56
- Aurière M, Lignières F, Konstantinova-Antova R, Charbonnel C, Petit P, Tsvetkova S, Wade G (2014) In: Mathys G, Griffin ER, Kochukhov O, Monier R, Wahlgren GM (eds) *Putting A stars into context: evolution, environment, and related stars*, pp 444–450. [arXiv:1310.6942](https://arxiv.org/abs/1310.6942)

- Babcock HW (1961) *ApJ* 133:572
- Bahng J, Schwarzschild M (1961) *Astrophys J* 134:312
- Baliunas SL, Donahue RA, Soon W, Henry GW (1998) *Cool stars, stellar systems, and the sun*, vol 154, pp 153
- Baliunas SL et al (1995) *Astrophys J* 438:269
- Bastien FA, Stassun KG, Basri G, Pepper J (2013) *Nature* 500:427
- Bastien FA et al (2014) *Astron J* 147:29
- Bedding TR et al (2001) *Astrophys J* 549:L105
- Berdugina SV (2005) *Living Rev. Solar Phys.* 2
- Berdugina SV, Usoskin IG (2003) *Astron Astrophys* 405:1121
- Bonfils X et al (2013) *Astron Astrophys* 549:A109
- Bouchy F, Bazot M, Santos NC, Vauclair S, Sosnowska D (2005) *Astron Astrophys* 440:609
- Bumba V, Ambroz P (1974) *Proc Int Astron Union* 56:183
- Catalano S, Biazzo K, Frasca A, Marilli E, Messina S, Rodonò M (2002) *Astronomische Nachrichten* 323:260
- Cegla HM et al (2012) *Mon Not R Astron Soc* 421:L54
- Chabrier G, Baraffe I (1997) *Astron Astrophys* 327:1039
- Chabrier G, Küker M (2006) *Astron Astrophys* 446:1027
- Charbonneau P (2010) *Living Rev Solar Phys* 7:3
- Choudhuri AR (2007) In: Hasan SS, Banerjee D (eds) *American institute of physics conference series. Kodai School on Solar Physics*, vol. 919, pp 49–73
- Cincunegui C, Díaz RF, Mauas PJD (2007) *Astron Astrophys* 469:309
- Collier Cameron A et al (2009) *Mon Not R Astron Soc* 400:451
- Collier Cameron A et al (2006) *Mon Not R Astron Soc* 373:799
- Cumming A (2004) *Mon Not R Astron Soc* 354:1165
- Del Moro D, Berrilli F, Duvall TLJ, Kosovichev AG (2004) *Solar Phys* 221:23
- Desort M, Lagrange AM, Galland F, Udry S, Mayor M (2007) *Astron Astrophys* 473:983
- Donati JF, Collier Cameron A (1997) *Mon Not R Astron Soc* 291:1
- Dravins D, Lindegren L, Nordlund A (1981) *Astron Astrophys* 96:345
- Dumusque X, Boisse I, Santos NC (2014) *ApJ* 796:132 [arXiv:1409.3594](https://arxiv.org/abs/1409.3594)
- Dumusque X et al (2012) *Nature*
- Dumusque X, Udry S, Lovis C, Santos NC, Monteiro MJPF (2010) *Astron Astrophys* 525:A140
- Duncan DK et al (1991) *Astrophys J Suppl Ser* 76:383
- Edelson RA, Krolik JH (1988) *Astrophys J* 333:646
- Ferraz-Mello S, Tadeu dos Santos M, Beaugé C, Michtchenko TA, Rodríguez A (2011) *Astron Astrophys* 531:A161
- Figueira P, Santos NC, Pepe F, Lovis C, Nardetto N (2013) *Astron Astrophys* 557:93
- Gilliland RL et al (2011) *Astrophys J Suppl Ser* 197:6
- Gizon L, Birch AC, Spruit HC (2010) *Annu Rev Astron Astrophys* 48:289
- Gizon L, Duvall TLJ, Larsen RM (2001) *Proc Int Astron Union* 203:189
- Gray DF (1989) *Astron Soc Pac* 101:832
- Gray DF (1992) *Camb Astrophys Ser*
- Hale GE (1908) *Astrophys J* 28:315
- Hall JC (2008) *Living Rev Solar Phys* 5:2
- Hall JC, Lockwood GW, Skiff BA (2007) *Astron J* 133:862
- Hansen CJ, Kawaler SD (1994) *Stellar interiors. Physical principles*
- Hathaway DH (2010) *Living Rev Solar Phys* 7:1
- Hatzes AP (1996) *Publ Astron Soc Pac* 108:839
- Hatzes AP et al (2010) *Astron Astrophys* 520:A93
- Hatzes AP (2011) *Astrophys J* 743:75
- Haywood RD et al (2014) *Mon Not R Astron Soc* 443(3):2517–2531, 443, 2517
- Henry TJ, Soderblom DR, Donahue RA, Baliunas SL (1996) *Astron J* 111:439
- Hirayama T (1978) *Publ Astron Soc Jpn* 30:337

- Högbom JA (1974) *Astron Astrophys Suppl Ser* 15:417
- Hussain G (2002) *Astronomische Nachrichten* 323:349
- Ivanov KG, Kharshiladze AF (2013) *Geomagn Aeron* 53:677
- Jeffers SV, Keller CU, Stempels E (2009) In: *Cool stars, stellar systems, and the sun* (AIP), pp 664–667
- Kjeldsen H, Bedding TR, Frandsen S, Dall TH (1999) *Mon Not R Astron Soc* 303:579
- Kraft RP (1967) *Astrophys J* 150:551
- Kuhn JR (1983) *Astrophys J* 264:689
- Labonte BJ, Howard R, Gilman PA (1981) *Astrophys J* 250:796
- Lagrange AM, Meunier N, Desort M, Malbet F (2011) *Astron Astrophys* 528:L9
- Lanza AF et al (2009) *Astron Astrophys* 493:193
- Lanza AF et al (2010) *Astron Astrophys* 520:A53
- Lanza AF, Boisse I, Bouchy F, Bonomo AS, Moutou C (2011) *Astron Astrophys* 533:A44
- Leighton RB (1959) *Astrophys J* 130:366
- Leighton RB, Noyes RW, Simon GW (1962) *Astrophys J* 135:474
- Lindegren L, Dravins D (2003) *Astron Astrophys* 401:1185
- Llama J, Jardine M, Mackay DH, Fares R (2012) *Mon Not R Astron Soc* 422:L72
- Lockwood GW, Skiff BA, Henry GW, Henry S, Radick RR, Baliunas SL, Donahue RA, Soon W (2007) *Astrophys J Suppl Ser* 171:260
- Lockwood GW, Skiff BA, Radick RR (1997) *Astrophys J* 485:789
- Lockwood M (2005) Solar outputs, their variations and their effects on Earth
- Lomb NR (1976) *Astrophys Space Sci* 39:447
- Lovis C et al (2011) *Astron Astrophys*, pre-print [arXiv:1107.5325](https://arxiv.org/abs/1107.5325)
- Makarov VV, Beichman CA, Catanzarite JH, Fischer DA, LEBRETON J, Malbet F, Shao M (2009) *Astrophys J* 707:L73
- Mallik SV (1996) *VizieR On-line Data Catalog* 412:40359
- Marcy GW et al (2014) *Astrophys J Suppl Ser* 210:20
- Martínez-Arnáiz R, Maldonado J, Montes D, Eiroa C, Montesinos B (2010) *Astron Astrophys* 520:A79
- Maunder EW (1904) *Mon Not R Astron Soc* 64:747
- McQuillan A, Mazeh T, Aigrain S (2014) *Astrophys J Suppl Ser* 211:24
- Meunier N, Desort M, Lagrange AM (2010) *Astron Astrophys* 512:A39
- Middelkoop F (1982) *Astron Astrophys* 107:31
- Miesch MS (2005) *Living Rev Solar Phys* 2:1
- Morin J et al (2008) *MNRAS* 384:77 [arXiv:0711.1418](https://arxiv.org/abs/0711.1418)
- Novotny E (1971) *An introduction to stellar atmospheres and interiors*. Oxford University Press, New York, 350 p, 1
- Noyes RW, Weiss NO, Vaughan AH (1984) *ApJ* 287:769–773. doi:[10.1086/162735](https://doi.org/10.1086/162735), <http://adsabs.harvard.edu/abs/1984ApJ...287..769N>
- Olah K, Panov KP, Pettersen BR, Valtaoja E, Valtaoja L (1989) *Astron Astrophys* 218:192
- Parker EN (1963) *ApJ* 138:226
- Pepe F et al (2013) *Nature* 503:377
- Perryman M (2011) *The exoplanet handbook* by Michael Perryman
- Petrovay K, van Driel-Gesztelyi L (1997) *Solar Phys* 176:249
- Queloz D et al (2009) *Astron Astrophys* 506:303
- Queloz D (2001) *Astron Astrophys* 379:279
- Radick RR, Lockwood GW, Skiff BA, Baliunas SL (1998) *Astrophys J Suppl Ser* 118:239
- Reiners A (2009) *Astron Astrophys* 498:853
- Reiners A (2012) *Living Rev Solar Phys* 9
- Roberts DH, Lehar J, Dreher JW (1987) *Astron J* 93:968
- Roberts WO (1945) *Astrophys J* 101:136
- Robinson RD, Boice DC (1982) *Solar Phys* 81:25
- Roudier T, Malherbe JM, Vigneau J, Pfeiffer B (1998) *Astron Astrophys* 330:1136

- Rutten RJ, Schrijver CJ (1994) NATO Adv Sci Inst (ASI) Ser C 433
- Saar S (1991) IAU Colloq. 130: the sun and cool stars. Act, Magn, Dyn 380:389
- Sanchis-Ojeda R, Winn JN (2011) *Astrophys J* 743:61
- Sanchis-Ojeda R, Winn JN, Holman MJ, Carter JA, Osip DJ, Fuentes CI (2011) *Astrophys J* 733:127
- Scargle JD (1982) *Astrophys J* 263:835
- Schrijver CJ (2002) *Astronomische Nachrichten* 323:157
- Schrijver CJ, Zwaan C (2000) Solar and stellar magnetic activity/Carolus J. Schrijver, Cornelius Zwaan. Cambridge astrophysics series, vol 34. Cambridge University Press, New York, 1
- Schwabe M (1844) *Astronomische Nachrichten* 21:233
- Sheeley NRJ (1967) *Astrophys J* 147:1106
- Skumanich A (1972) *Astrophys J* 171:565
- Solanki SK (2002) *Astronomische Nachrichten* 323:165
- Solanki SK (2003) *Astron Astrophys Rev* 11:153
- Soltau D (1993) In: The magnetic and velocity fields of solar active regions. Astronomical society of the Pacific conference series; Proceedings of the international astronomical union (IAU) colloquium no. 141, held in Beijing, China, 6–12 September 1992. Astronomical Society of the Pacific (ASP), San Francisco, pp 225
- Spiegel EA, Zahn J-P (1992) *Astron Astrophys* 265:106
- Spruit HC (1976) *Solar Phys* 50:269
- Strassmeier KG (2009) *Astron Astrophys Rev* 17:251
- Strassmeier KG, Washuettl A, Schwöpe A (2002) *Astronomische Nachrichten* 323:155
- Stumpe MC et al (2012) *Publ Astron Soc Pac* 124:985
- Thomas JH, Weiss NO (2008) Sustainability, 1
- Tobias SM (2002) *Philos Trans R Soc A: Math, Phys Eng Sci* 360:2741
- Toner CG, Gray DF (1988) *Astrophys J* 334:1008
- Vaughan AH, Preston GW, Wilson OC (1978) *Publ Astron Soc Pac* 90:267
- Vogt SS, Penrod GD (1983) *Publ Astron Soc Pac* 95:565
- Voigt H-H (1956) *Zeitschrift für Astrophysik* 40:157
- Walder R, Folini D, Meynet G (2012) *Space Sci. Rev.* 166:145
- Walkowicz LM et al (2011) *Astron J* 141:50
- Weiss LM, Marcy GW (2014) *Astrophys J* 783:L6
- Wilson OC (1963) *Astrophys J* 138:832
- Wilson OC (1968) *Astrophys J* 153:221
- Wilson OC (1978) *Astrophys J* 226:379
- Zechmeister M, Kürster M (2009) *Astron Astrophys* 496:577
- Zirin H (1966) A Blaisdell book in the pure and applied sciences. Blaisdell, Waltham, 1

Radial-velocity Searches for Planets Around Active Stars

Haywood, R.D.

2016, XV, 140 p. 60 illus., 57 illus. in color., Hardcover

ISBN: 978-3-319-41272-6